# Chapter 3: Synthesis of Materials and Experimental Procedure

This chapter provides a comprehensive overview of the experimental procedures, and the techniques employed to fabricate and characterize the porous $Cu$ current collector designed for use in advanced LMB. The section highlights the various methods and parameters utilized to optimize both the printing and sintering processes, which are crucial for ensuring the performance and stability of the fabricated current collectors. Additionally, this chapter details the characterization techniques that were implemented to analyse the morphological features of the lithium deposition on the porous Cu current collectors, which is a key aspect of evaluating their functionality in electrochemical applications.

## 3.1 Material Synthesis

### 3.1.1 Material Selection

$Cu$ powder with a 99% purity procured from Nano Matrix, India, was selected as the primary material. This high-quality $Cu$ powder was chosen for its potential to enhance the performance and functionality of the printed product. To prepare the ink with a high loading of $Cu$ particles, a combination of binder and solvents was used. The binder used in this process was PLA 4060 D grade, sourced from Nature Works, USA while the solvents employed include Dichloromethane, Dibutyl Phthalate, and 2-Butoxyethanol, all of which were procured from Thermo Fisher Scientific.

The particle distribution of the Cu powder is depicted in Fig 3.1 b, where it can be observed that 90% of the $Cu$ particles are smaller than 1 $\mu m$ in diameter. The particle size distribution ranges from 0.4 $\mu m$ to 4.51 $\mu m$, showcasing a relatively narrow spread of particle sizes. This fine and consistent distribution plays a critical role in the overall performance of the product.

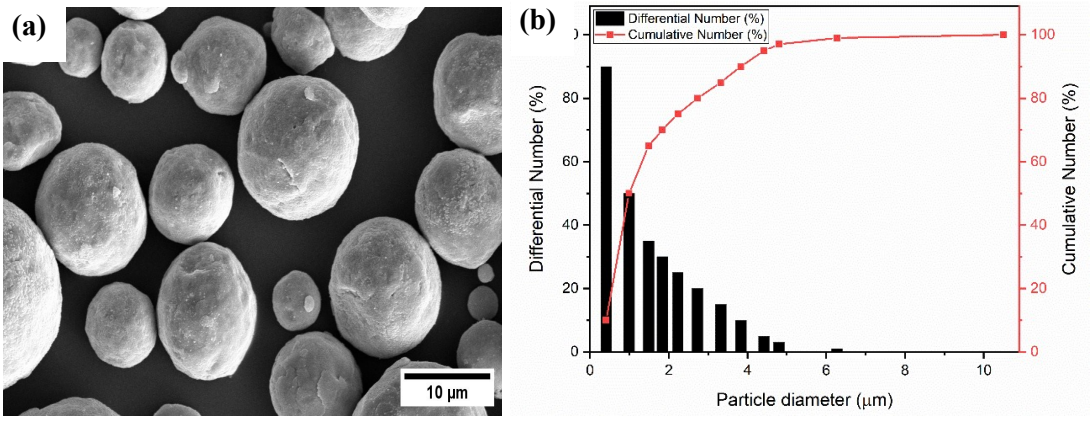


Fig. 3.1: (a) SEM showing spherical $Cu$ particle (b) Distribution curve of the spherical $Cu$ particles

As evidenced by the SEM image shown in Fig. 3.1(a), the $Cu$ particles exhibit a spherical morphology. The choice of small, spherical $Cu$ powder was intentional, as this specific particle shape and size were selected to achieve optimal particle mobility and uniform distribution throughout the ink. The spherical shape minimizes friction between the particles, thus facilitating smoother extrusion through the printing nozzle. This characteristic is essential for ensuring a continuous and consistent printing process, which is crucial for achieving high-quality results [107].

Furthermore, the small size and spherical shape of the $Cu$ particles contribute significantly to the printed product's surface quality and apparent density. The smaller particles help to enhance the surface finish of the printed material, reducing the presence of defects and improving the overall smoothness and uniformity of the surface. This, in turn, leads to an increase in the apparent density of the printed product, ensuring that the material has desirable mechanical properties and structural integrity. The choice of materials, particle size, and binder composition all contribute to the improved functionality and performance of the ink and the final printed product, making this approach highly suitable for advanced additive manufacturing applications.

### 3.1.2 Ink Preparation

The detailed procedure for preparing the ink is illustrated in Fig. 3.2. The first step in the process involves preparing a solvent mixture consisting of Dichloromethane (DCM), Dibutyl Phthalate, and 2-Butoxyethanol, which are combined in an appropriate ratio to form a homogeneous solution. PLA is dissolved in DCM & $Cu$ powder is dissolved in a solvent and the complete mixture is mixed in a vortex mixture followed by ultra-sonication.

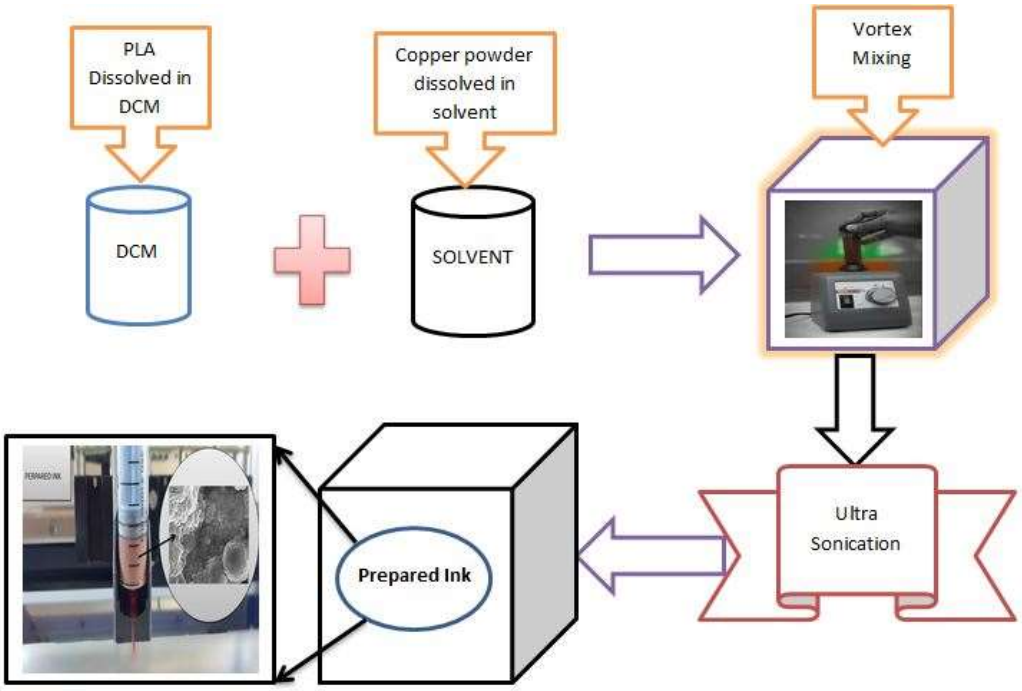


Fig. 3.2: Schematic for the preparation of the ink

This solvent mixture plays a crucial role in ensuring proper dispersion of the $Cu$ powder and binder in the final ink. The solvent combination was carefully selected to optimize the solubility and dispersion characteristics, allowing for effective particle suspension. Next, a separate suspension was prepared by dissolving PLA in DCM. This step ensures that the PLA binder is effectively dissolved in the solvent, forming a consistent liquid phase that can later incorporate the $Cu$ powder. Once the PLA and DCM suspension was prepared,

the $Cu$ powder was added to the suspension mixture. The addition of $Cu$ powder was done gradually to avoid clumping or premature aggregation of the particles. The primary purpose of incorporating the $Cu$ powder at this stage is to achieve a uniform suspension of the metallic particles in the binder and solvent mixture.

To ensure that the $Cu$ powder, PLA binder, and solvent were thoroughly mixed, vortex mixing was employed. The mixing process was carried out using a Vortex Mixer (Remi CM 101 Plus, India, as shown in Fig. 3.3 (b), which provided high shear forces that helped to break up any particle aggregates and ensure uniform dispersion throughout the mixture. This step was essential for achieving a homogenous ink mixture, where the $Cu$ particles were evenly distributed within the binder solution, preventing clumping or sedimentation.

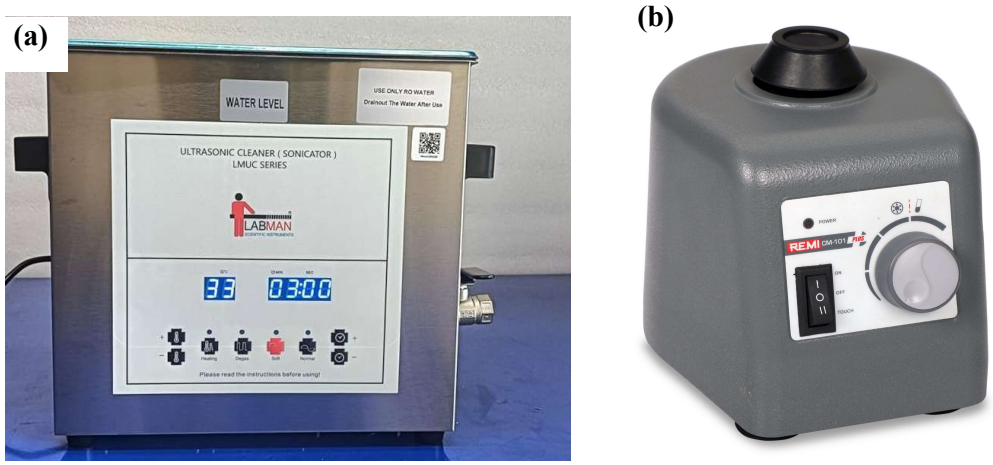


Fig. 3.3: (a)Ultrasonicator (b) Vortex Mixture

Following the initial mixing, the next step involved the removal of the solvent, DCM, and the homogenization of the suspension to achieve a stable and uniform ink. This was achieved through ultrasonic sonication using a Labman Ultrasonicator bath (5L, China) as shown in Fig. 3.3 (a). The ultrasonic bath was operated for 1 h, during which high-frequency sound waves were applied to the suspension. The cavitation effect generated by the ultrasound waves helps in breaking down any remaining particle agglomerates,

ensuring that the $Cu$ particles were uniformly dispersed throughout the mixture. After the sonication process, the result was a homogeneous $Cu$ ink mixture with no visible aggregation or clumping of particles. The ink exhibited excellent stability and uniformity, making it ideal for use in additive manufacturing processes. The thorough preparation process ensures that the ink can be smoothly extruded through the nozzle, providing a high-quality finish for the printed products.

In summary, the ink preparation process involves multiple steps: the careful preparation of the solvent mixture, dissolution of the binder, addition of $Cu$ powder, vortex mixing, and final homogenization through ultrasonic sonication. Each of these steps was designed to ensure that the final $Cu$ ink mixture was uniform, stable, and ready for use in advanced printing applications.

## 3.2 Experimental Procedure

### 3.2.1 Viscosity Measurement

The viscosity measurement is done using ARES $G_2$ (TA Instruments, USA) advanced rotational rheometer as shown in Fig. 3.4. When using the ARES $G_2$ to measure viscosity and other rheological properties, selecting the appropriate geometry and setting precise experimental conditions are essential for obtaining accurate and reliable results. Typically, plate diameters of 25 mm or 40 mm are used, which are standard for many types of samples, particularly for liquids or pastes with moderate viscosities. The gap between the plates is generally set around 500 µm, but it can be adjusted depending on the consistency and nature of the sample being tested, such as the viscosity of different ink formulations. A well-controlled gap ensures consistent shear conditions and minimizes errors in viscosity measurement.

Fig. 3.4: ARES $G_2$ advanced rotational rheometer

In terms of temperature control, the ARES $G_2$ provides two main options: the Peltier Plate or the Forced Convection Oven (FCO). These methods allow for precise temperature regulation during measurements, which is particularly important when analysing materials like inks, as their viscosity can change significantly with temperature. The temperature range for these measurements typically spans from 25°C to 80°C, depending on the specific formulation of the ink or material being studied. Controlling the temperature is essential to understand how viscosity changes in response to different environmental conditions, and it helps simulate real-world application conditions for materials.

When measuring viscosity, the shear rate sweep is commonly used to analyze the material's behavior under varying flow conditions. This technique applies a shear rate range from 0.01 $s^{-1}$ to 1000 $s^{-1}$, which is suitable for both Newtonian and non-Newtonian fluids. The sweep provides insight into how the material's viscosity changes with shear rate, revealing important characteristics such as shear thinning or thickening behavior, which are crucial in understanding flow properties in applications such as printing, coating, or mixing.

For more complex materials, particularly those that exhibit viscoelastic behavior, the frequency sweep in oscillatory mode is a critical test. In this mode, the rheometer applies an oscillatory shear to the sample at frequencies ranging from 0.1 Hz to 100 Hz. This frequency range allows for the examination of the material's viscoelastic properties, including its storage modulus (G'). The frequency sweep is used to determine how the material behaves under different oscillatory conditions, providing insights into its elasticity and viscosity at varying time scales. The strain applied during the test typically ranges from 0.1% to 5%, ensuring that the material remains within the linear viscoelastic region. This range helps ensure that the material's response is purely elastic or viscous without causing non-linear or yielding effects, making the data more reliable for characterizing the material's intrinsic rheological properties.

### 3.2.2 Direct ink writing

The $Cu$ inks, formulated with optimal rheological properties, were utilized in the fabrication of the desired parts. To begin the process, a detailed computer-aided design (CAD) model was created, representing the final product according to the required specifications. This CAD model was then converted into the. STL format, which is compatible with the machine's interfacing software, enabling the system to interpret and execute the printing process with precision. The schematic of the complete process has been shown in Fig. 3.5.

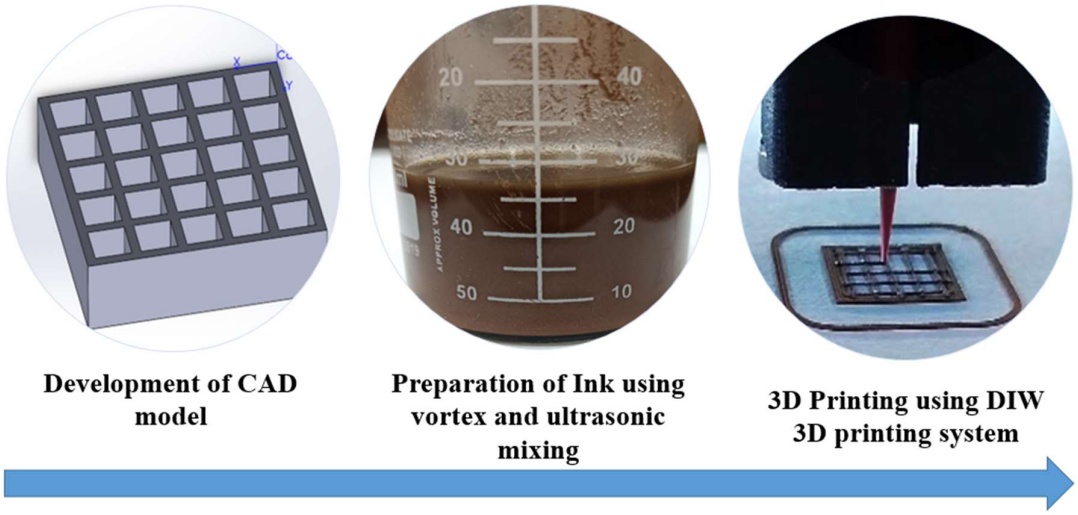


Fig. 3.5: Flow chart for the 3D printing of the green sample

The 3D printing was carried out using a DIW system, specifically a multimaterial extrusion-based 3D printer (Make: Hyrel 3D, USA shown in Fig. 3.6). This system is well-suited for the deposition of materials like the prepared $Cu$ ink. The ink, carefully formulated to achieve the necessary rheological properties for smooth extrusion, was loaded into a 30 ml plastic syringe. The syringe was outfitted with a micro nozzle having a diameter of 200 $\mu m$, designed to accurately deposit the $Cu$ ink in precise amounts during the printing process.

A schematic representation of the entire 3D printing process is illustrated in Fig. 3.5. The printing process was carried out with the optimized speed, ensuring steady material deposition throughout the build. Moreover, a controlled flow rate was maintained to ensure the ink was extruded systematically and uniformly through the nozzle. This enabled the creation of detailed and accurate 3D $Cu$ structures layer by layer.

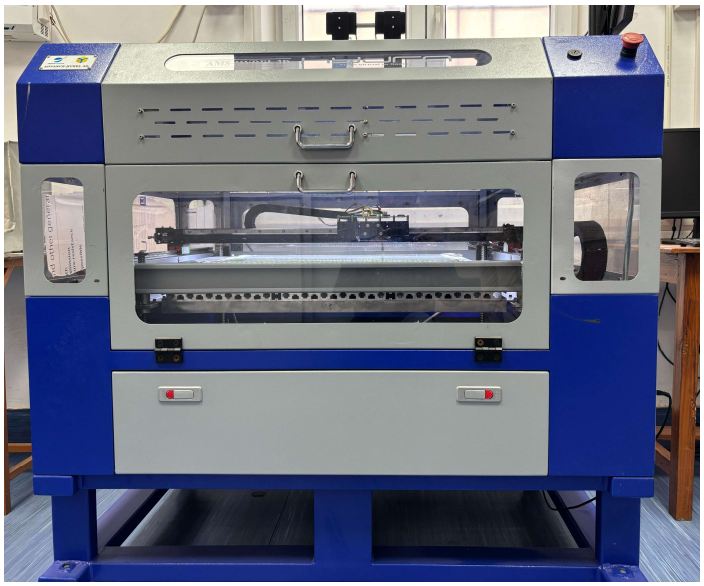

Fig. 3.6: Hyrel 3D Ceramic Printer

Following the deposition of each underlying layer of the $Cu$ ink, the nozzle was carefully shifted along the Z-axis to the appropriate height, ensuring proper alignment for the subsequent layer. This layering process continued until the complete 3D structure was successfully fabricated.

Once the 3D-printed $Cu$ parts, known as green $Cu$ samples, were completed, they were left to dry at room temperature for 24 h. This drying step was crucial for allowing any excess solvent within the ink to evaporate, stabilizing the printed structure before any additional post-processing or sintering steps were to be performed.

### 3.2.3 Sintering Process

The debinding and sintering of the 3D-printed green $Cu$ samples were carried out using a tube sintering furnace (Make: Ants Innovation, India shown in Fig. 3.7), a critical step to achieve the desired properties of the $Cu$ parts after the initial 3D printing. The process began with the placement of the fully dried green $Cu$ samples inside the tube of the sintering furnace. Once the sample was securely positioned, the flanges of the tube furnace were closed to seal it, ensuring no external air could interfere with the process.


Fig. 3.7: Tube Sintering furnace

To begin the debinding and sintering cycle, a vacuum was generated within the furnace tube to create a controlled atmosphere. The vacuum was carefully reduced to a pressure of $10^{-3}$ Torr, effectively removing the air from the tube and minimizing the risk of unwanted reactions during the subsequent stages of the process. Once the desired vacuum level was reached, the tube was purged with Ar gas to further stabilize the environment inside the furnace. The Ar gas was supplied at a flow rate of 121 $mm^3$/min, ensuring that the atmosphere inside the tube was refreshed approximately every 30 s. This constant gas flow prevents the build-up of any undesirable gases, contributing to the integrity of the sintering process. Following the successful completion of the gas purging stage, the heating cycle within the tube furnace was initiated. The sintering process was carefully controlled using a two-step heating cycle, designed to address both the debinding and sintering of the $Cu$ particles. The complete steps starting from 3D printing to preparation of the final sample has been shown in Fig. 3.8.

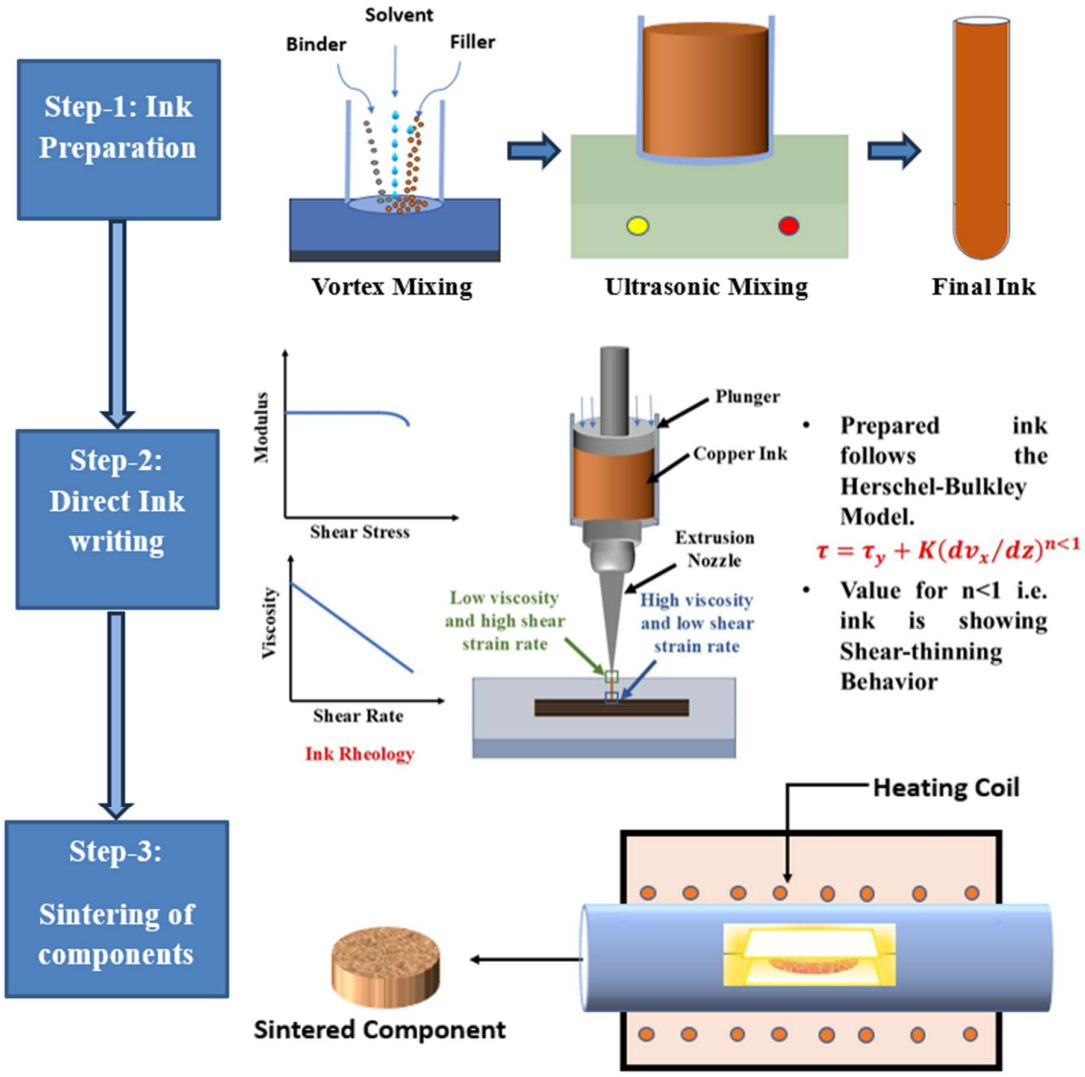


Fig. 3.8: Schematic of the complete process for the preparation of the final component

The first step of the cycle focused on the debinding process, where the organic components or binders present in the green $Cu$ samples were removed. This is a crucial step as the binder is required to hold the $Cu$ particles together during the 3D printing process, but it must be removed prior to sintering to ensure that the final product has the correct material properties. The debinding was carried out at a temperature of 350°C for a soaking time of 3 h, which is consistent with values previously reported for the debinding of other materials

like PLA. During this step, the heat causes the binder to degrade and evaporate, leaving behind only the $Cu$ particles that are ready for sintering.

Once the debinding step was completed, the second stage of the cycle, sintering, was initiated. Sintering involves the fusion of individual $Cu$ particles, bringing them closer together to form a solid, cohesive structure. The sintering temperature for the $Cu$ particles was set at 980°C, which is just below the melting point of $Cu$, allowing the particles to bond without causing the material to melt. The sintering step lasted for 1 h, providing sufficient time for the diffusion of $Cu$ particles at the elevated temperature to achieve strong inter-particle bonds and a dense, solid structure. Throughout both the debinding and sintering steps, the heating rate was varying from 2-6°C per minute, ensuring a gradual and controlled increase in temperature. This controlled heating rate helps avoid thermal shock to the materials and ensures uniform temperature distribution, which is critical for achieving optimal material properties.

After the completion of the two-step sintering cycle, the heating was stopped, and the samples were allowed to cool within the furnace. The cooling process took place in the controlled environment of the Ar atmosphere, which helps prevent oxidation or other forms of contamination during the cooling stage. The parts were left inside the furnace until they reached room temperature, completing the sintering process and ensuring that the final $Cu$ structures possessed the desired mechanical and structural properties.

In summary, the debinding and sintering process of the 3D-printed green $Cu$ samples was meticulously controlled, involving careful vacuum and gas purging, a precise two-step heating cycle, and a controlled cooling phase. These steps ensured the successful conversion of the green $Cu$ samples into fully sintered $Cu$ parts with enhanced density, strength, and stability.

### 3.2.3.1 Plan for experiments

In the present research, Central Composite Design (CCD) technique was used for planning of the experimentation. The selected range of process parameters for the study has been shown in Table 3.1

**Table 3.1- Process parameters ranges and levels**

| $Symbol$/Levels | -2 | -1 | 0 | 1 | 2 |
|---|---|---|---|---|---|
| $X_1$ $(Sintering\ Temp)$ (℃) | 650 | 750 | 850 | 950 | 1050 |
| $X_2$ ( $Heating\ Rate$ ) (℃/$min$ ) | 2 | 3 | 4 | 5 | 6 |
| $X_3$ $(Soaking\ Time)$ $(min)$ | 30 | 45 | 60 | 75 | 90 |

Regarding sintering temperature, a range between 650 ℃ to 1050 ℃ was chosen. It was found from preliminary experimentation that sintering of green $Cu$ sample was achieved after 600 ℃. However, a large amount of inherent porosity was found in these samples. Hence, a higher temperature for sintering was also examined and a sintering temperature of 1050 ℃ was found to be feasible for sintering with higher densification. After 1050 ℃, the melting and oversintering of $Cu$ particles was observed. Similarly, below 650 ℃, poor densification was obtained. Hence, this range for sintering temperature was selected. Furthermore, the heating rate range between 2-6 ℃/$min$ selected considering machine limitations and preliminary experimentation results. Pertaining to soaking time, the lower range of 30 min was chosen as it yields better surface diffusion during the sintering process. For higher range of soaking time, 90 min was selected as above this range no considerable impact on the compressive strength was observed.

A total of 20 experiments were planned for obtaining the optimized set of sintering parameters. The 20 experiments were designed for the ($\alpha = 2$) according to response surface method (RSM).

$$Y = \beta_0 + \sum_{i=1}^{k} \beta_i X_i + \sum_{i=1}^{k} \beta_i X_i^2 + \sum \beta_{ij} X_i X_j + \varepsilon \quad \text{..... (3.1)}$$

Where $Y$ represents the response variable and $k$ denotes that how many variables were used. $\beta$ is the constant and $\varepsilon$ denotes the error constant and $Xi$, $Xi^2$ ,and $XiXj$ denotes the 1st, 2nd order, and the interaction of the parameters. Subsequently, the optimization of the sintering parameters was performed using Genetic Algorithm (GA) technique to achieve maximum value of relative density, minimum value of volumetric shrinkage and high value of compressive strength.

### 3.2.3.2 Statistical Modelling

The experiments that were performed were shown in Table 3.2 along with input and the output parameters. The results were analyzed using the $ANOVA$ method. The parameters having p values more than 0.05 were considered as insignificant parameters and these parameters were excluded from the output variables to analyze the impact of significant parameters. In order to make the statistical analysis, a regression study was performed. The equation 3.2 to 3.4 shows the statistical equations for the RD, $\sigma_y$ and $V$.

$$RD = 19.1 + 0.1566 \times X_1 - 6.41 \times X_2 + 0.2733 \times X_3 - .000091 \times X_1 \times X_1 - 0.497\, X_2 \times X_2 - .001876 \times X_3 \times X_3 + .00719 \times X_1 \times X_2 \quad \text{.....(3.2)}$$

$$\sigma_y = 11.5 + 0.376 \times X_1 - 38.1 \times X_2 + 0.1185 \times X_3 - 0.000257 \times X_1 \times X_1 - 1.305 \times X_2 \times X_2 + 0.0391 \times X_1 \times X_2 \quad \text{.....(3.3)}$$

$$V = -83.5 + 0.1791 \times X_1 + 3.20 \times X_1 + 0.3733 \times X_3 - 0.000079 \times X_1 \times X_1 - 0.396 \times X_2 \times X_2 - 0.002265 \times X_3 \times X_3 - 0.00439 \times X_1 \times X_2 \quad \text{.....(3.4)}$$

The 95 % confidence level was used for the calculations of $ANNOVA$ and confirmation experiments were performed to validate the statistical model.

**Table 3.2- Input parameters and responses**

| S. No. | $Sintering\ Temperature$ (℃) | $Heating\ Rate$ ($℃/min$) | $Soaking\ Time$ ($min$) | $Relative\ density$ $RD$ (%) | $Compressive\ strength$ $\sigma_y$ (MPa) | $Volumetric\ Shrinkage$ $V$ (%) |
|---|---|---|---|---|---|---|
| **1.** | 750 | 3 | 45 | 86.68 | 115.42 | 13.23 |
| **2.** | 950 | 3 | 45 | 91.35 | 130.64 | 20.43 |
| **3.** | 750 | 5 | 45 | 75.78 | 74.93 | 8.78 |
| **4.** | 950 | 5 | 45 | 84.87 | 106.78 | 13.45 |
| **5.** | 750 | 3 | 75 | 88.89 | 121.25 | 18.34 |
| **6.** | 950 | 3 | 75 | 92.78 | 132.63 | 25.78 |
| **7.** | 750 | 5 | 75 | 77.93 | 81.56 | 10.13 |
| **8.** | 950 | 5 | 75 | 85.11 | 107.61 | 15.59 |
| **9.** | 650 | 4 | 60 | 77.38 | 84.43 | 9.32 |
| **10.** | 1050 | 4 | 60 | 89.32 | 118.71 | 18.97 |
| **11.** | 850 | 2 | 60 | 92.94 | 135.46 | 23.32 |
| **12.** | 850 | 6 | 60 | 76.47 | 77.79 | 8.14 |
| **13.** | 850 | 4 | 30 | 83.63 | 104.98 | 12.42 |
| **14.** | 850 | 4 | 90 | 86.68 | 111.56 | 18.13 |
| **15.** | 850 | 4 | 60 | 86.79 | 112.45 | 16.93 |
| **16.** | 850 | 4 | 60 | 86.48 | 111.57 | 16.34 |
| **17.** | 850 | 4 | 60 | 87.87 | 112.89 | 17.62 |
| **18.** | 850 | 4 | 60 | 86.17 | 110.45 | 17.16 |
| **19.** | 850 | 4 | 60 | 86.53 | 114.89 | 18.45 |
| **20.** | 850 | 4 | 60 | 87.48 | 117.74 | 17.36 |

### 3.2.4 Compression Test

The mechanical strength of 3D-printed sintered samples was rigorously evaluated through a compressive strength test. The testing was performed using the Instron 25 kN Nano Load Universal Testing Machine (UTM), specifically the BI-7000 model, which is renowned for its precision and capability to measure both small and large forces accurately. Fig. 3.9 shows the compression test of 3D printed cylinder. This machine was ideal for evaluating

the compressive properties of the samples, providing high-resolution data on load and displacement during the test.

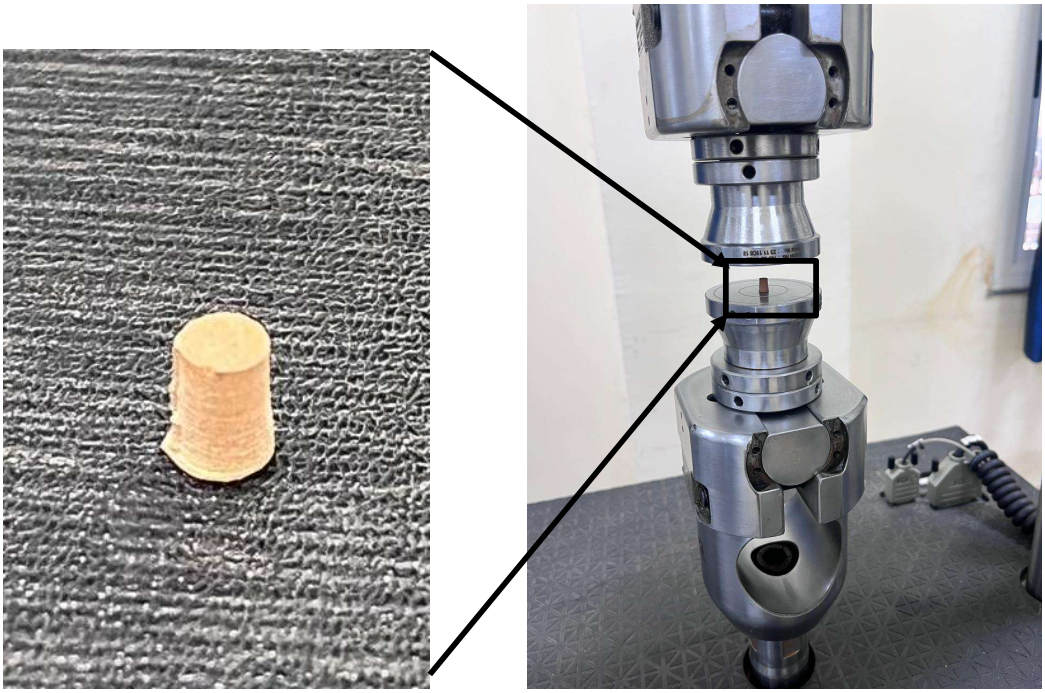

Fig. 3.9: Compression test of 3D printed Cylinder

The compressive strength test was conducted on cylindrical samples that were fabricated using optimized process parameters. These parameters were carefully chosen to ensure the best balance of material integrity and performance during the sintering process, which is crucial for achieving accurate and repeatable mechanical properties. The cylinders, with a diameter of 5 mm and a height of 7.5 mm, were designed with an L/D ratio of 1.5, which is a typical configuration for such tests and aligns with standard testing practices for cylindrical samples. This design ensures that the sample undergoes uniform compression and provides reliable data regarding the material's behavior under load.

The stroke rate during the compression test was set at 1 mm/min, a standard rate for compression testing that ensures the material’s response to stress is captured gradually. This stroke rate allows for precise measurement of the material's deformation as the applied

force increases, ensuring that any potential failure or yielding is documented in detail. The applied load was varied between 0 and 3000 N, covering a wide range of forces to examine the sample's behavior across different stress levels. For each increment of applied load, the corresponding displacement was continuously recorded, providing detailed data on how the material deforms under compression.

Additionally, the compression tests were conducted in accordance with the ASTM E09 standard, which outlines the procedures for testing the compressive properties of materials, particularly for cylindrical specimens. This ensures that the results are in line with industry best practices and that the compressive strength values obtained are both accurate and comparable to other material testing results in the field.

The combination of optimized sample preparation, precise testing conditions, and adherence to ASTM standards allows for a thorough and reliable evaluation of the compressive strength of the 3D-printed sintered samples, providing valuable insights into their mechanical properties and suitability for various engineering applications.

### 3.2.5 Electrochemistry & Characterization

Coulombic efficiency tests were systematically carried out to evaluate the charge and discharge cycles of the fabricated half coin cells, providing essential insights into their electrochemical performance and stability over multiple cycles. These charge-discharge experiments were conducted using the Arbin 20084 battery tester (manufactured in the USA), a high-precision instrument designed for characterizing battery cells under controlled conditions. The focus of these tests was to monitor the performance of the half coin cells, which were of the CR2032 type, a widely used format in electrochemical testing, ensuring reliable and reproducible results.

To guarantee the integrity of the samples and to prevent any unwanted reactions with moisture or oxygen, the entire assembly process of the half coin cells took place inside a glovebox. This glovebox maintained a highly controlled inert atmosphere, typically containing argon or nitrogen, ensuring that the electrodes and electrolytes remained shielded from any environmental contaminants that could affect their performance, such as water vapor or atmospheric oxygen. Such precautionary measures are critical in lithium-based systems, where even minimal exposure to air or moisture could lead to undesirable side reactions or degradation of the materials. Fig. 3.10 shows the complete schematic for the fabrication of the coin cell using direct ink writing and sintering.

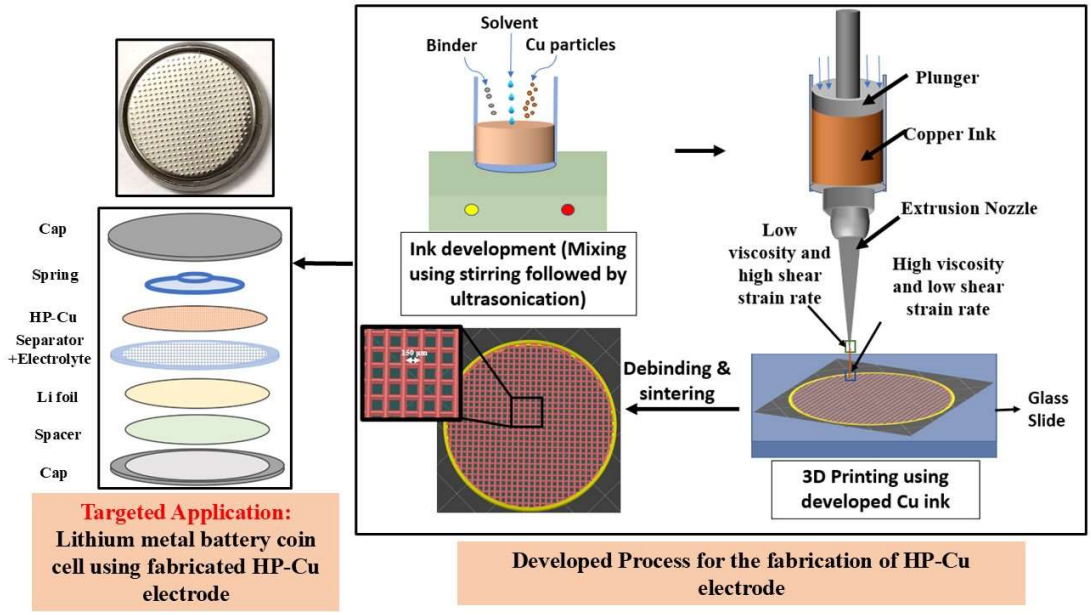


Fig. 3.10: Procedure for the fabrication of 3D printed HP-$Cu$ current collector for LMB

The electrolyte used in these tests was a carefully formulated solution consisting of 1,3-dioxolane (DOL) and 1,2-dimethoxyethane (DME), mixed with lithium bis(trifluoromethane)sulfonimide (LiTFSI) as the lithium salt, and 1 wt% $LiNO_3$. The inclusion of $LiNO_3$ played a vital role in enhancing the overall performance and stability of the half coin cells. $LiNO_3$ is known to promote the formation of a robust SEI layer on the

anode, which helps mitigate ongoing side reactions between the lithium metal anode and the electrolyte. This is crucial as the SEI layer acts as a protective barrier, stabilizing the anode surface and preventing excessive decomposition of the electrolyte. Additionally, the nitrate ions present in the electrolyte foster the formation of passivation layers that inhibit uneven lithium deposition during cycling, ensuring more uniform plating and stripping of lithium. The careful selection of this specific electrolyte composition was aimed at optimizing both the electrochemical performance and the longevity of the half coin cells.

The coulombic efficiency of the cells was calculated over a voltage range of -0.5 V to +0.5 V, a range specifically chosen to capture the full dynamics of the lithium plating and stripping processes. These processes are central to the functioning of lithium-based batteries, where the deposition and dissolution of lithium ions at the anode during cycling are critical factors in determining both efficiency and cycle life. By operating within this voltage window, the test could effectively monitor the charge-discharge cycling efficiency, assessing how well the half coin cells could reversibly store and release charge over repeated cycles.

Following the completion of the plating and stripping cycles, the electrodes were meticulously cleaned to remove any residual electrolyte or byproducts that might have accumulated during the testing process. This cleaning was performed using 1,2-dimethoxyethane (DME), a solvent that is compatible with the electrolyte and ensures thorough removal of any contaminants without compromising the electrode's surface integrity. After cleaning, the electrodes were carefully dried within the glovebox to maintain the inert atmosphere, preventing any exposure to external contaminants such as oxygen or moisture.

To gain a deeper understanding of the electrochemical behavior of the electrodes, especially in relation to the performance of the 3D-printed HP-$Cu$ current collector, the cleaned electrodes were transferred to a SEM for detailed surface analysis. The transfer of the electrodes to the SEM required careful handling to preserve the inert atmosphere and prevent exposure to air, which could alter the material's properties. A custom-designed holder was employed to facilitate this transfer without disrupting the controlled environment of the glovebox. This holder was specifically crafted to ensure that the electrodes remained within the same inert atmosphere during the transition from the glovebox to the SEM's vacuum chamber, preserving the integrity of the sample for accurate imaging.

The SEM analysis allowed for a comprehensive examination of the surface morphology and microstructural features of the 3D-printed HP-$Cu$ current collector. This innovative current collector design was the primary focus of the study, as the researchers sought to evaluate its performance in comparison to the traditional $Cu$ foil commonly used in battery applications. By examining the surface of the current collector at high resolution, the SEM provided valuable insights into the structural characteristics, such as the uniformity of the current collector's surface, potential defects, and how these factors might influence the electrochemical performance.

In addition to the SEM analysis, further structural characterization was conducted using X-ray diffraction (XRD). The XRD analysis was carried out using a HR-XRD machine (Rigaku-SmartLab: 9kW), which utilized $Cu$ Kα radiation. XRD is an essential technique for identifying the crystalline phases and structural properties of materials. By analyzing the diffraction patterns, researchers were able to gain insights into the crystalline structure of the HP-$Cu$ current collector and how its properties might differ from conventional

materials, providing additional context for the electrochemical performance observed during the charge-discharge cycles.

To further evaluate the internal resistance and charge transfer dynamics of the half coin cells, impedance spectroscopy was performed following the cycling tests. This technique provides valuable information about the electrochemical impedance of the cell, which reflects the internal resistance and the ease with which charge can be transferred across the electrolyte and electrodes. The impedance measurements were conducted with a disturbance amplitude of 5 mV, and the frequency range spanned from 1 MHz to 1 Hz, allowing for a detailed analysis of the cell's performance across a broad range of time scales. The data obtained from the impedance tests helped identify key factors affecting the overall performance, including resistance to ion flow, charge transfer efficiency, and the stability of the SEI layer.